Capacitive Deionization of Saline Water by Using MoS_2-Graphene Hybrid Electrodes with High Volumetric Adsorption Capacity

Jinlong Han,[§,†] Tingting Yan,[§,†] Junjie Shen,[‡] Liyi Shi,[†] Jianping Zhang[†] and Dengsong Zhang*[,†]

[†] Department of Chemistry, College of Sciences, State Key Laboratory of Advanced Special Steel, Research Center of Nano Science and Technology, School of Materials Science and Engineering, Shanghai University, Shanghai 200444, PR China.

[‡] Department of Chemical Engineering, University of Bath, Bath BA2 7AY, UK.

* Corresponding authors: E-mail: dszhang@shu.edu.cn.

[§] J.H. and T.Y. contributed equally to this work.

ABSTRACT: Capacitive deionization (CDI) has received wide attention as an emerging water treatment technology due to its low energy consumption, low cost and high efficiency. However, the conventional carbon electrode materials for CDI have low densities, which occupy large volumes and are disadvantageous for use in limited space (e.g., in household or on offshore platforms). In order to miniaturize the CDI device, it is quite urgent to develop high volumetric adsorption capacity (VAC) electrode materials. To overcome this issue, we rationally designed and originally developed high VAC MoS_2-graphene hybrid electrodes for CDI. It is interesting that MoS_2-graphene hybrid electrode has a much higher NaCl volumetric adsorption capacity of 14.3 mg/cm^3 with a gravimetric adsorption capacity of 19.4 mg/g. It has been demonstrated that the adsorption capacity is significantly enhanced due to the rapid ion transport of MoS_2 and high electrical conductivity of graphene. *In-situ* Raman spectra and high-angle annular dark-field scanning transmission electron microscopy tests demonstrated a favorable Faradaic reaction, which was crucial to enhancing the NaCl volumetric adsorption capacity of MoS_2-graphene hybrid electrode. This work opens a new avenue for

miniaturizing future CDI devices.

■ INTRODUCTION

With the growth of population and the development of industry, human beings consume a large amount of fresh water resources.[1] The widespread water scarcity and water contamination problems are seriously increasing across the world, threatening human health and ecological integrity.[2-5] In coastal areas, desalination of saline water is an important way to obtain fresh water.[6] Conventional desalination methods include reverse osmosis thermal distillation and electrodialysis.[7-9] They have demonstrated a variety of disadvantages in practical applications, such as high energy consumptions and high economic costs.[10]

As an emerging water treatment technology, capacitive deionization (CDI) has gained increasing attention due to its prominent advantages, such as high efficiency, low cost, low energy consumption and easy operations and ease of maintenance.[11-13] The principle of CDI is analogous to that of the electrical double-layer capacitor:[14] When exposed to an external electric field, the charged ions in the feed water move towards the oppositely charged electrode by electrostatic attraction and are adsorbed and/or trapped on the surface of electrodes accompanied by simultaneous energy storage, thus the deionized water is produced in the outlet. When the electric field is reversed or the electrodes were short-circuited, the ions adsorbed in the electrodes are released, accompanied by the release of energy stored in the electrodes, therefore the electrodes are regenerated. Various CDI models and techniques, such as flow electrode capacitive deionization, membrane capacitive deionization, faradaic CDI and hybrid CDI have attracted increasing attention in the last decade.[9,15-17]

Electrode materials are vital for the CDI performance. Key features of an excellent electrode material include high electrical conductivity, high adsorption capacity, reasonable pore structure, high

chemical and mechanical stability, environmentally friendly, and favorable water wettability.[18] Traditional electrode materials used in CDI, including activated carbon (AC), porous carbon, carbon fibers, carbon cloths, carbon nanotubes and graphene have been extensively studied due to their high chemical stability, high electrical conductivity and high adsorption capacity.[19] In recent years, some materials with pseudocapacitance such as TiO_2, MnO_2, MoS_2，some molybdate and phosphate attracted a lot of attentions.[20-22] Despite great efforts have been devoted to preparing novel CDI electrode materials,[23-25] most of current studies are focused on the enhancement of the gravimetric adsorption capacity (GAC, mg/g) while little attention has been paid to the enhancement of the volumetric adsorption capacity (VAC, mg/cm^3). Traditional carbonaceous electrodes are relatively low in density, such as only 0.4-0.6 g/cm^3 for activated carbon and 1-2 g/cm^3 for multiwall carbon nanotubes.[26] The utilization of low density materials leads to its low VAC, which is unfavorable when the CDI devices are used in a limited space (e.g., in household or on offshore oil/gas platforms).[27] Therefore, enhancing the VAC of the CDI electrodes is a major objective for future CDI development.

MoS_2 is one of the most interesting two-dimensional layered materials, in which two layers of sulfur atoms are sandwiched by a layer of molybdenum atoms. Each three-layer structure is connected by a weak Van Der Waals force, which gives MoS_2 a variety of fascinating properties such as large surface area, high density and fast ionic conductivity.[28] Specifically, the density of MoS_2 is around 4-5 g/cm^3, which is much higher than that of carbon materials.[29] Combining the high electrical conductivity of graphene with the high density of MoS_2 may result in a highly conductive and compact electrode material for CDI.

Herein, we rationally designed and originally developed a novel hybrid MoS_2-graphene electrode for CDI applications (Figure 1a and 1b). The MoS_2-graphene electrode showed a high NaCl adsorption

capacity (VAC_{NaCl}) as well as a high NaCl adsorption capacity (GAC_{NaCl}), as a result of the high electrical conductivity of graphene and the rapid ion transport of MoS_2. This study reveals a new avenue for miniaturizing future CDI devices.

■ EXPERIMENT

Preparation. Graphene oxide (GO, 99.5%, Graphene-king Company, Shanghai, China), ammonium molybdate tetrahydrate ($(NH_4)_6Mo_7O_{24}\cdot 4H_2O$) and thiourea were purchased from Aladdin (Shanghai, China). All the chemicals were analytically pure and not purified further. MoS_2-graphene hybrid electrodes were synthesized through a simple *in-situ* growth strategy (Figure 1b). Typically, 1.12 g thiourea and 40 mg graphene oxide (dispersed in DI water, 2 mg/mL) were dissolved in 75 mL water under vigorous stirring to make a homogenous mixture. Then 4 g $(NH_4)_6Mo_7O_{24}\cdot 4H_2O$ was added into the mixture under stirring for 30 min followed by transferring into the 100 mL Teflon-lined stainless autoclave and hydrothermally treated at 170 ºC for 12 h. Afterward, the sediment was separated by suction filtration and washed by absolute ethanol and DI water followed by drying at 60 ºC at ambient air. At last, the resultant powder was calcined at 600 ºC with a ramping rate of 5 ºC /min under a flowing argon atmosphere. Samples with graphene oxide additive amount of 0, 40, 60, 80, 100 and 200 mg were named by MoS_2, MG-0.8, MG-1.2, MG-1.6, MG-1.9 and MG-3.8, respectively.

Characterization. Scanning electron microscope (SEM, Hitachi S-4800) and transmission electron microscope (TEM, JEM 2100) were used to observe the morphological and structural properties of the samples. The phase compositions were determined using the X-ray diffractometer (XRD, Cu Kα, 40 kV, 20 mA). Raman spectroscopy were investigated by a spectrometer with a 633 nm Ar^+ laser and *in-situ* Raman spectra of whole cyclic voltammetry (CV) cycle between 0.5 V and -0.5 V were conducted on a Raman spectrometer (HORIBA scientific, LabRAM HR Evolution, France)

with a 633 nm laser. Nitrogen isothermal adsorption-desorption curves were investigated (Autosorb-IQ2, America). The specific surface area and the pore size distribution were determined by the Brunauer–Emmett–Teller (BET) method and the Barrett–Joyner–Halenda (BJH) and density Functional Theory (DFT) model, respectively. Water wettability was evaluated by drop shape analysis using Kruss, DSA100 instrument. Electrochemical performance was evaluated through an electrochemical workstation (CHI 660D, Chenhua, Shanghai). The working electrode was fabricated through mixing of polytetrafluoroethylene (PTFE) aqueous dispersion and active material with a ratio of 1: 9 in weight and shaped into 1 cm square film. The CV and galvanostatic charge-discharge (GCD) curves and electrochemical impedance spectroscopy (EIS) were measured in a 0.5 M NaCl solution with a three-electrode system. The calomel electrode and graphite film serve as reference electrode and counter electrode, respectively. The capacitance is calculated by the equation (1)

$$C = \frac{\int I dV}{2mv\Delta V} \quad (1)$$

Where C is the capacitance (F/g), I is the response current density (A), m is the mass of active material (g), υ is the scanning rate (V/s), and ΔV is the applied voltage window during the cyclic voltammetry test (V). The proportion of contribution of capacitive charge and the diffusion-controlled charge were calculated according to the equation (2).[30]

$$i(V) = k_1 v + k_2 v^{0.5} \quad (2)$$

Where the i is the current (A), the v is the scanning rate (mV/s), k_1 and k_2 are constant values at a fixed potential. $k_1 v$ is related to the capacitive current raised from electrical double layer (EDL) and $k_2 v^{0.5}$ is related to diffusion-controlled charge.

Batch-Mode CDI Experiments. The electrode for batch-mode CDI experiments was fabricated through adequate mixing of the PTFE, conductive carbon black and as-prepared active

111 material with a ratio of 1:1:8 in weight, then was shaped into 65 mm square film and casted onto the
112 graphite film current collector. An asymmetric electrode system was assembled using as-prepared
113 electrode and graphite film (GF) as the working electrode and the counter electrode (GF‖MG-1.6
114 electrode pairs), respectively. The other asymmetric electrode was assembled using as-prepared
115 electrode and graphite film loaded with activated carbon as the working electrode and the counter
116 electrode (AC‖MG-1.6 electrode pairs), respectively. The homemade device (Figure 1a) was used to
117 examine the salt adsorption performance as demonstrated in previous work by our group.[31,12] The two
118 CDI electrodes was separated by placing a spacer between them. A 50 mL NaCl solution was driven
119 cyclically through the electrodes via a peristaltic pump. A conductivity meter (SevenMulti, METTLER
120 TOLEDO, America) was used to monitor the conductivity of the NaCl solution online. When it is
121 necessary to compare the variations of solution conductivity in different batch-mode test, the initial
122 solution conductivity is normalized just for comparative purposes to eliminate the system error. In this
123 work, graphite film loaded with as-prepared material was used as cathode, graphite film or graphite
124 film loaded with activated carbon was used as anode. The GAC was calculated in theory by the
125 equation (3):

126 $$GAC = GAC_T - GAC_{NA} \quad (3)$$

127 Where the *GAC* is gravimetric adsorption capacity (mg/g), the GAC_T is the total *GAC* obtained by
128 CDI tests of the whole electrodes (mg/g), the GAC_{NA} is the premeasured *GAC* of non-active materials
129 (mg/g). For CDI test with GF‖MG-1.6 electrode pairs, Na^+ ions gravimetric adsorption capacity
130 (GAC_{Na}) was used to evaluate the ability of deionization of active materials, which was calculated by
131 the equation (4) as follow.

132 $$GAC_{Na} = \frac{0.394(C_{NA} - C_T)V}{M} \quad (4)$$

Where 0.394 is the mass fraction of sodium in NaCl, C_{NA} is the NaCl aqueous solution concentration during the desalination test of non-active material (mg/L) (Figure S1), C_T is the NaCl aqueous solution concentration during the desalination test of the as-prepared electrodes (mg/L), M is the quality of as-prepared electrode material (g) and V is volume of NaCl solution (L). The thickness of active material film is calculated by follow equation (5):

$$T_{af} = T_t - T_{cc} \quad (5)$$

Where T_{af} is active material film thickness (μm), T_t is average total thickness (μm), T_{cc} is average current collector (graphite film) thickness (μm). Both the T_{cc} and T_t are measured by micrometer (Figure S3). The Na^+ volumetric adsorption capacity (VAC_{Na}) was calculated by the equation (6):

$$VAC_{Na} = \frac{GAC_{Na} \times M}{T_{af} \times a} \quad (6)$$

Where a is the area of active electrode film on the current collector (cm^2), respectively. For the CDI test with AC‖MG-1.6 electrode pairs, the GAC_{NaCl} was calculated by the equation (7) as follow.

$$GAC_{NaCl} = \frac{(C_{NA} - C_T)V}{m_t} \quad (7)$$

Where m_t is the quality of total mass both cathode and anode electrode material (g). The NaCl VAC_{NaCl} was calculated by the equation (8):

$$VAC_{NaCl} = \frac{GAC_{NaCl} \times m_t}{aT_{af} + bT_{AC}} \quad (8)$$

Where b is activated carbon film area (cm^2), T_{AC} is activated carbon film thickness (cm). The T_{AC} was calculated adopted similar method with T_{af}. Average Na^+ adsorption rate ($ASAR_{Na}$) ($mg/cm^3/min$) was calculated by equation (9):

$$ASAR_{Na} = \frac{0.394V \int_0^t (C_{NA}(t) - C_T(t))dt}{T_{af} \times a \times t} \quad (9)$$

Where $C_{NA}(t)$ and $C_T(t)$ is instant concentration of the NaCl aqueous solution during the deionization (mg/L), t is the time of deionization (min). During the regeneration of the electrode, the external

direct voltage was removed and the work electrode was directly connected with the counter electrode by a copper wire.

The regeneration tests were conducted at a flow rate of 60 mL/min and a direct voltage of 1.2 V. The initial conductivity of the NaCl solution was 200 μS/cm. When the electrodes were regenerated, they were connected by wire directly to release the adsorbed ions.

■ RESULTS AND DISCUSSION

Structure and Composition Analysis. The morphologies of the obtained materials were demonstrated by TEM and SEM images. Figure 1c-d show the SEM images of the MG-1.6. There are a large number of MoS_2 pleats on the surface of the particles and these protrusions are uniform and interlaced in a flaky shape, which is advantageous for increasing the specific surface area. According to the TEM (Figure 1e-1f) and HRTEM (Figure 1g) images of MG-1.6, it can be clearly observed that a large number of MoS_2 sheets are homogenously distributed on the surface of the graphene, which is conducive to increase the conductivity of electrode. The lattice spacing was calculated to be 0.68 nm (Figure 1g), corresponding to the (002) lattice plane of the hexagonal MoS_2.[32] The thickness of the MoS_2 layer of MG-1.6 is calculated to be 9 nm corresponding to layers number of 14, which contributes to increase conductivity of the MoS_2-graphene hybrid electrode. It was found that as the additive amount of graphene oxide increases, the agglomeration of the sheet-like MoS_2 on graphene is alleviated and the sheet becomes smaller with a better dispersion (Figure S2). When the additive amount of graphene oxide is more than 1.9 wt%, the MoS_2 sheets cannot be clearly distinguished (Figure S2f). This result is possibly due to the fact that graphene provides nucleation sites for the formation of MoS_2,[33,34] and an increase in the amount of graphene makes the nucleation rate surpass the growth rate, resulting in a reduction in the size of MoS_2 sheets. However, too small MoS_2 crystals

177 are not beneficial to preventing graphene stacking. Conversely, the highly agglomerated MoS_2 is
178 unfavorable for mass transfer, because the number of adsorption sites is limited.

179 The phase properties of different samples were examined by XRD (Figure 2a). The obvious
180 diffraction peaks located at 13.7°, 33.6° and 59.9° correspond to the (002), (100) and (008) planes of
181 hexagonal MoS_2 (JCPDS, No. 37-1492), respectively, indicating good crystalline nature of MoS_2. That
182 is favorable to the chemical stability of electrode. Actually, the peaks located at 26°, 37.0° and 53.5°
183 in the Figure 2a are corresponding to (011), (020) and (022) planes of MoO_2 (JCPDS 65-5787).[35] MoO_2
184 is produced because the $(NH_4)_6Mo_7O_{24}\cdot 4H_2O$ is excessive and the thiourea is insufficient. The
185 excessive molybdate ions were transformed into MoO_2. As the electrical resistivity of MoO_2 (10^{-5} Ω
186 cm^{-1}) is much lower than that of MoS_2 (~1 Ω cm^{-1}), therefore MoO_2 is beneficial for conductivity of
187 the as-prepared materials.[36,37]

188 The specific surface areas calculated from N_2 adsorption-desorption isotherms (left of Figure 2b)
189 for MG-0.8, MG-1.2, MG-1.6, MG-1.9, MG-3.8 are 27.2, 28.9, 37.9, 35.3 and 34.2 m^2/g, respectively.
190 The results implied that the content of graphene affects the specific surface area significantly. Low
191 content of graphene makes MoS_2 agglomerated and excessive graphene makes itself stacked. The
192 hysteresis curves include a hysteresis loop at a high-pressure stage, and the area of the hysteresis loop
193 is related to the pore volume.[38] According to the pore size distribution profiles (right of Figure 2b and
194 Figure S4), MG-1.6 has the large portions of mesopores, indicating their superior mass transfer
195 capacities. Moreover, the good hydrophilicity of MG-1.6 has been demonstrated (Figure S5), which
196 favors the CDI process for the practical applications.

197 The Raman spectra were conducted to examine the structure and topology of the MoS_2-graphene
198 and the layer number (Figure 2c and 2d). The peaks located at 378 cm^{-1} and 405 cm^{-1} are corresponding

to E^1_{2g} and A_{1g} peaks, respectively.[20] E^1_{2g} peak is assigned to the in-plane displacement in Mo and S atoms and A_{1g} is assigned to the out-plane symmetric displacement of S atom along the c-axis.[39] As shown in Figure 2d, a slight blue-shift of A_{1g} is found, indicating the layer number of MoS_2 decreasing,[40,41] which accounts the effect of inhibition on layer number of MoS_2 by graphene. The peak located at around 1360 cm^{-1} and 1580 cm^{-1} are corresponding to the D and G peaks of graphene (Figure 2c), which arise from the sp^3-hybridized carbon and the sp^2-hybridized carbon.[42] The increasing intensity of D and G peaks indicates the increase of graphene content, moreover, the D peak is larger than G peak demonstrating the small degree of graphitization.

Electrochemical Performance. The GCD test was implemented to examine the capacitance of the as-prepared samples (Figure 3a). The results show that MG-1.6 has the longest discharge time at 0.2 A/g, implying that it possesses the largest capacitance among all the electrodes. The sample MG-1.6 was tested at different current densities (Figure S6a). The result shows that it keeps a long discharge time of 150 s at a large current density of 1.0 A/g. The extent of IR drop is positively related to the inner electrical resistance of the electrodes.[12,43] The IR drop of MG-1.6 displays the smallest IR drop (the inset of Figure 3a), indicating that it has the smallest inner electrical resistance. The result is due to the preferable distribution of MoS_2 particles of MG-1.6 on the graphene, ensuring a high electrical conductivity and a small internal resistance. The IR drops at different current densities are shown in Figure S6b. The result confirms that the IR drop increases linearly with the increase of current density, which is attributed to the inadequate discharge in the EDL at the onset of discharge. A superior charge-discharge performance and a good cyclic stability of 10 000 cycles are obtained for MG-1.6 electrode (Figure 3d).

The CV test for exploring the electrochemical behavior in a 0.5 M NaCl solution shows the

rectangular-like closed curve of MG-1.6 (Figure S6c), suggesting good capacitor characteristics.[44] As calculated from the area of the rectangular curves, the capacitances of MG-1.6 is 146.1 F/g at a scanning rate of 5 mV/s, which is higher than other contrast samples (Figure S6d), implying remarkable adsorption capacity. The capacitances of MG-1.6 at different scanning rates are shown in Figure S6e. The MG-1.6 still has a capacitance of 47.9 F/g even at a high scan rate of 50 mV/s, which is due to the good electrical conductivity of MG-1.6. Two redox peaks at 1 mV/s (Figure S6f) demonstrates the existence of a redox process. The proportion of contribution of capacitive charge and the diffusion-controlled charge were calculated according to the equation (2). CV curves at 0.2 mV/s and 0.5 mV/s have been measured, respectively. Based-on the equation (2), at a given potential *P*, two known different current values i_1 and i_2 are obtained at two scanning rates v_1 (0.2 mV/s) and v_2 (0.5 mV/s), thus obtaining a binary equations as follow.

$$i_1(P) = 0.2\mathrm{k}_1 + \sqrt{0.2}\mathrm{k}_2 \quad (10)$$

$$i_2(P) = 0.5\mathrm{k}_1 + \sqrt{0.5}\mathrm{k}_2 \quad (11)$$

k_1 and k_2 at *P* potential can be obtained by solving the above binary equations consisting equation (10) and (11). A CV cycle contains a series of potential values, so a series of k_1 and k_2 values can be obtained. For the same material, k_1 and k_2 are fixed at a given potential. Therefore, at the scanning rate of 0.2 mV/s, the current derived from electric double-layer capacitor can be obtained by the equation (12).

$$i_{EDLC}(V) = 0.2 \times k_1 \quad (12)$$

Where i_{EDLC} is the current derived from electric double-layer capacitor. These i_{EDLC} points can be linked to form a closed CV curve, which is the shaded part in Figure 3b. The area of shaded part as a percentage of the area of the measured CV curve is the percentage of the contribution of the electric

double layer capacitor. The rest is the diffusion-controlled charge contribution. The shadow area is corresponding to the capacitive current at 0.2 mV/s (Figure 3b), which takes a proportion of 72.7%. The result demonstrates that capacitive charge contributes 72.7% of the capacity and the diffusion-controlled charge contributes 27.3% of capacity.

The EIS test for examining the resistance of the as-prepared samples (Figure 3c) shows that each curve has a similar shape which consists of a pressed and rotated semi-circle and a slope line. The pressed and rotated semi-circle is related with the interface resistance between the surface of electrode and the electrolyte bulk. The slope line correlates to the ion diffusion on the surface of electrode.[45,46] It was found that MG-1.6 has relatively small diameter of semicircle, revealing small charge transfer resistance. The result may be attributed to the high conductivity of MG-1.6 arising from the homogenous distribution of MoS_2 particles on the surface of graphene. The slope line correlates with the capacitor characteristics and a greater slope of the line means more capacitor characteristics. The inset of Figure 3c shows a relative larger slope line of MG-1.6, suggesting better capacitor characteristics.

CDI Performance. Figure 4a shows the Ragone plots of average salt adsorption rate ($ASAR_{Na}$) *versus* (*vs.*) VAC_{Na} of different samples. The result displays that MG-1.6 made the largest decrease of normalized solution conductivity (Figure S8a) and had the largest VAC_{Na} up to 6.0 mg/cm^3 and it maintained a high salt adsorption rate even at the high VAC_{Na} stage, which is attributed to the improved microstructure of graphene on MoS_2. Compared to activated carbon, MG-1.6 can save 54% volume at the same adsorption capacity (Table S1). Figure 4b shows the plots of GAC *vs.* deionization time, and Figure 4c shows the plots of VAC_{Na} *vs.* deionization time. It is found that GAC_{Na} of MG-1.6 reached to 8.1 mg/g, and still kept a relatively high deionization rate at the high VAC_{Na} stage. The high GAC_{Na}

and VAC_{Na} should be attributed to the good ions transfer channel of MG-1.6 resulting from the large fraction of mesopores. GAC_{Na} and deionization rate can be facilitated by favorable pore size distribution. Mesopore is very beneficial to decrease transfer resistance and provides superior ions transfer channel, so that the consumed ions can be replenished quickly from bulk solution, thus very favorable for enhancing deionization capacity. To compared with some reported literatures in the same calculation method, a batch-mode CDI test using the AC ‖ MG-1.6 electrode pairs were carried out (Figure S7a and S7b). The calculation methods of VAC_{NaCl} and GAC_{NaCl} have taken into account the effect of current collectors and both the cathode and anode electrode materials mass. The VAC_{NaCl} and GAC_{NaCl} were calculated to 14.3 mg/cm^3 and 19.4 mg/g, respectively. Compared to the reported literatures, the VAC_{NaCl} reaches high level and GAC_{NaCl} is also slightly superior (Figure 4d and S7c, Table 1 and S2).[25,47-55] The GAC_{Na} and $ASAR_{Na}$ at different flow rates were studied (Figure S8b and S8c) and the results show negligible difference among the applied flow rates, implying no obvious impact on GAC_{Na} and $ASAR_{Na}$ and exhibits good stability under different flow rates. Performance of MG-1.6 at different direct voltages was investigated (Figure S9a, S9b and S9c) and a high VAC_{Na} was acquired at 1.2 V. The effect of the initial concentration of NaCl solution on GAC_{Na}, VAC_{Na}, and $ASAR_{Na}$ was studied (Figure S10a, S10b and S10c) and the result shows that both GAC_{Na} and VAC_{Na} increases with the rising initial concentration. The pH value change was investigated during the desalination and regeneration (Figure S11a and S11b). The change of pH may be due to the decomposition of local water.[56] MG-1.6 also display good performance to remove the heavy metal ions. At low concentration of 0.31 mmol/L Cu^{2+} aqueous solution, the removal rate of Cu^{2+} by MG-1.6 reached to 92.3% (Figure S12a). While, at low concentration of 0.48 mmol/L Pb^{2+} aqueous solution, the removal rate of Pb^{2+} by MG-1.6 reached to 91.3% (Figure S12b). A good regeneration ability of

MG-1.6 was examined in 100 mg/L NaCl aqueous solution at 1.2 V and 60 mL/min and showed good regeneration stability up to 50 CDI cycles (Figure S13). These results are because of good chemical stability and capacitor characteristics of MG-1.6.

In-situ Raman spectra were conducted for exploring the mechanism of Na-ions storage of MoS_2 (Figure S14). The results show the ratio of characteristic peaks, E^1_{2g}/A_{1g}, of 2H MoS_2 decreased with potential decrease from 0 V to -0.5 V at the start stage and increase during the potential increased from -0.5 V to 0.5 V, then decrease during the potential decrease from 0.5 V to 0 V at the end of the whole CV cycle (Figure 5a, Table S3). This result is related with Na^+ insertion reaction in the interlayers of MoS_2 as follow.

$$Na^+ + xe^- + MoS_2 \rightarrow Na_xMoS_2 \quad (13)$$

Because Raman peak A_{1g} is sensitive to interlayer electron density. The binding to electrons during the faradaic reaction (13) lead to increasing the interlayer electron density of MoS_2, resulting in a decrease in A_{1g} strength and an increase in E^1_{2g}/A_{1g}.[57,58]

In order to more clearly prove the phase transformation from 2H MoS_2 to 1T MoS_2, HAADF-STEM was conducted to observe the atom array. A mixed phase in the area was founded indicating the co-existence of 2H and 1T MoS_2 after 50 CDI cycles (Figure 5c). Before CDI cycles of the regeneration test, the as-prepared electrode was characterized by Raman spectra and no peaks of 1T MoS_2 was found (Figure 5b). However, after 50 CDI cycles, the characteristic peaks of 1T MoS_2 were found at 150 and 233 cm^{-1} corresponding to the known J1 and J2 peaks.[59-61] Therefore, an inference that the 2H MoS_2 partly transferred to 1T MoS_2 is reasonable (Figure 5d). For NaCl removal using AC ‖ MG-1.6 electrode pairs, the whole deionization process is described below. Firstly, Na^+ migrates to polarized cathode under electrostatic force and adsorbed on the surface of the electrode. Then, some Na^+ ions

were embedded in the interlayer of MoS_2, and Faradaic reaction (13) occurs and MoS_2 changed from 2H phase to 1T phase. Simultaneously, Cl^- ions were adsorbed into the electrical double layers between the carbon surface and the bulk NaCl solution. The final material saturates sodium. In the regeneration stage, Na^+ and Cl^- ions adsorbed in the surface electric double-layer are first released. Then, the Na^+ ions embedded in the MoS_2 layer reacts (14) inversely, and some MoS_2 transforms into 2H phase, while others remain 1T phase. As for the reasons of partial phase transition, more in-depth study is needed. For CDI, we first use HAADF-STEM to study the phase composition in hybrid MoS_2-graphene CDI electrodes. The high VAC_{NaCl} electrodes prepared in this study present a promising approach to miniaturizing CDI devices for future applications.

■ ASSOCIATED CONTENT

Supporting information

Non-active materials deionization plots, TEM images, thickness of T_t and T_{cc}, dynamic water contact angle analysis. GCD, CV curves, IR drop and capacitance of different samples. Plots of GAC_{NaCl}, VAC_{NaCl} and NSC *vs.* time for MG-1.6 using AC ‖ MG-1.6 electrode pairs. Plots of NSC *vs.* time for different samples with graphite film as counter electrodes. Plots of NSC, VAC_{Na}, GAC_{Na} *vs.* time for MG-1.6 using GF ‖ MG-1.6 electrode pairs under different condition. Plots of removal of heavy metal ions, NSC and pH *vs.* time, regeneration plots using GF ‖ MG-1.6 electrode pairs. *In-situ* Raman spectra of a CV cycle, comparison of MoS_2-graphene hybrid electrodes and AC electrodes, comparison tables of AC electrode, peaks ratio, reported materials and this work.

■ AUTHOR INFORMATION

* E-mail: dszhang@shu.edu.cn.

■ ACKNOWLEDGEMENTS

This work was supported by the National Key R&D Program of China (2017YFB0102200), the

National Natural Science Foundation of China (21722704 and 21906101), and the Science and Technology Commission of Shanghai Municipality (16DZ1204300, 15DZ2281400 and 16JC1401700). We are grateful to Dr. Lupeng Han and Dr. Zaheen Ullah Khan for providing the helpful guidance. We are grateful to Dr. Hu Pengfei and Dr. Peng Jianchao, Test Center of Shanghai University, for providing the helpful guidance.

■ REFERENCES

(1) Harris-Lovett, S. R.; Binz, C.; Sedlak, D. L.; Kiparsky, M.; Truffer, B. Beyond User Acceptance: A Legitimacy Framework for Potable Water Reuse in California. *Environ. Sci. Technol.* **2015,** *49*, 7552-7561.

(2) Pekel, J. F.; Cottam, A.; Gorelick, N.; Belward, A. S. High-Resolution Mapping of Global Surface Water and Its Long-Term Changes. *Nature* **2016,** *540*, 418-422.

(3) Oki, T.; Kanae, S. Global Hydrological Cycles and World Water Resources. *Science* **2006,** *313*, 1068-1072.

(4) Konig, M.; Escher, B. I.; Neale, P. A.; Krauss, M.; Hilscherova, K.; Novak, J.; Teodorovic, I.; Schulze, T.; Seidensticker, S.; Hashmi, M. A. K.; Ahlheim, J.; Brack, W. Impact of Untreated Wastewater on A Major European River Evaluated with A Combination of in Vitro Bioassays and Chemical Analysis. *Environ. Pollut.* **2017,** *220*, 1220-1230.

(5) Barzen-Hanson, K. A.; Davis, S. E.; Kleber, M.; Field, J. A. Sorption of Fluorotelomer Sulfonates, Fluorotelomer Sulfonamido Betaines, and A Fluorotelomer Sulfonamido Amine in National Foam Aqueous Film-Forming Foam to Soil. *Environ. Sci. Technol.* **2017,** *51*, 12394-12404.

(6) Elimelech, M.; Phillip, W. A. The Future of Seawater Desalination: Energy, Technology, and The Environment. *Science* **2011,** *333*, 712-717.

(7) Westerhoff, P.; Atkinson, A.; Fortner, J.; Wong, M. S.; Zimmerman, J.; Gardea-Torresdey, J.; Ranville, J.; Herckes, P. Low Risk Posed by Engineered and Incidental Nanoparticles in Drinking Water. *Nat. Nanotechnol.* **2018,** *13*, 661-669.

(8) Pan, C.; Troyer, L. D.; Catalano, J. G.; Giammar, D. E. Dynamics of Chromium(VI) Removal from Drinking Water by Iron Electrocoagulation. *Environ. Sci. Technol.* **2016,** *50*, 13502-13510.

(9) Chang, Y.; Deng, L.; Meng, X. Y.; Zhang, W.; Wang, C. Z.; Wang, Y. X.; Zhao, S.; Lin, L.; Crittenden, J. C. Closed-Loop Electrochemical Recycling of Spent Copper(II) from Etchant Wastewater Using A Carbon Nanotube Modified Graphite Felt Anode. *Environ. Sci. Technol.* **2018,** *52*, 5940-5948.

(10) Surwade, S. P.; Smirnov, S. N.; Vlassiouk, I. V.; Unocic, R. R.; Veith, G. M.; Dai, S.; Mahurin, S. M. Water Desalination Using Nanoporous Single-Layer Graphene. *Nat. Nanotechnol.* **2015,** *10*, 459-464.

(11) Zhang, J.; Fang, J. H.; Han, J. L.; Yan, T. T.; Shi, L. Y.; Zhang, D. S. N, P, S Co-Doped Hollow Carbon Polyhedra Derived from MOF-Based Core-Shell Nanocomposites for Capacitive Deionization. *J. Mater. Chem. A* **2018,** *6*, 15245-15252.

(12) Tang, W. W.; Kovalsky, P.; Cao, B. C.; Waite, T. D. Investigation of Fluoride Removal from Low-Salinity Groundwater by Single-Pass Constant-Voltage Capacitive Deionization. *Water Res.* **2016,** *99*, 112-121.

(13) He, D.; Wong, C. E.; Tang, W. W.; Kovalsky, P.; Waite, T. D. Faradaic Reactions in Water Desalination by Batch-Mode Capacitive Deionization. *Environ. Sci. Tech. Let.* **2016,** *3*, 222-226.

(14) Khan, Z. U.; Yan, T. T.; Shi, L. Y.; Zhang, D. S. Improved Capacitive Deionization by Using 3D Intercalated Graphene Sheet-Sphere Nanocomposite Architectures. *Environ. Sci.: Nano* **2018,** *5*, 980-

991.

(15) Tang, W. W.; He, D.; Zhang, C. Y.; Waite, T. D. Optimization of Sulfate Removal from Brackish Water by Membrane Capacitive Deionization (MCDI). *Water Res.* **2017,** *121*, 302-310.

(16) He, C.; Ma, J. X.; Zhang, C. Y.; Song, J. K.; Waite, T. D. Short-Circuited Closed-Cycle Operation of Flow-Electrode CDI for Brackish Water Softening. *Environ. Sci. Technol.* **2018,** *52*, 9350-9360.

(17) Tang, W. W.; Kovalsky, P.; He, D.; Waite, T. D. Fluoride and Nitrate Removal from Brackish Groundwaters by Batch-Mode Capacitive Deionization. *Water Res.* **2015,** *84*, 342-349.

(18) Tang, K. X.; Chang, J. J.; Cao, H. B.; Su, C. L.; Li, Y. P.; Zhang, Z. S.; Zhang, Y. Macropore- and Micropore-Dominated Carbon Derived from Poly(Vinyl Alcohol) and Polyvinylpyrrolidone for Supercapacitor and Capacitive Deionization. *ACS Sustain. Chem. Eng.* **2017,** *5*, 11324-11333.

(19) Liu, P. Y.; Yan, T. T.; Shi, L. Y.; Park, H. S.; Chen, X. C.; Zhao, Z. G.; Zhang, D. S. Graphene-Based Materials for Capacitive Deionization. *J. Mater. Chem. A* **2017,** *5*, 13907-13943.

(20) Jia, F. F.; Sun, K. G.; Yang, B. Q.; Zhang, X.; Wang, Q. M.; Song, S. X. Defect-Rich Molybdenum Disulfide as Electrode for Enhanced Capacitive Deionization from Water. *Desalination* **2018**, *446* , 21-30.

(21) Peng, S. J.; Li. L. L.; Wu, H. B.; Madhavi, S.; Lou, X. W. Controlled Growth of $NiMoO_4$ Nanosheet and Nanorod Arrays on Various Conductive Substrates as Advanced Electrodes for Asymmetric Supercapacitors. *Adv. Energy. Mater.* **2015**, *5*, 1401172.

(22) Yu, X. Y.; Yu, L.; Lou, X. W. Hollow Nanostructures of Molybdenum Sulfides for Electrochemical Energy Storage and Conversion. *Small Methods* **2017**, *1*, 1600020

(23) Xu, X. T.; Wang, M.; Liu, Y.; Lu, T.; Pan, L. K. Metal-Organic Framework-Engaged Formation of A Hierarchical Hybrid with Carbon Nanotube Inserted Porous Carbon Polyhedra for Highly

Efficient Capacitive Deionization. *J. Mater. Chem. A* **2016,** *4*, 5467-5473.

(24) Chmiola, J.; Largeot, C.; Taberna, P. L.; Simon, P.; Gogotsi, Y. Monolithic Carbide-Derived Carbon Films for Micro-Supercapacitors. *Science* **2010,** *328*, 480-483.

(25) Xing, F.; Li, T.; Li, J. Y.; Zhu, H. R.; Wang, N.; Cao, X. Chemically Exfoliated MoS_2 for Capacitive Deionization of Saline Water. *Nano Energy* **2017,** *31*, 590-595.

(26) Clark, R. M. Evaluating The Cost and Performance of Field-Scale Granular Activated Carbon Systems. *Environ. Sci. Technol.* **1987**, *21*, 573-580.

(27) Gogotsi, Y.; Simon, P. True Performance Metrics in Electrochemical Energy Storage. *Science* **2012,** *335*, 167-167.

(28) Huang, K. L.; Wang, L.; Liu, Y. J.; Liu, Y. M.; Wang, H. B.; Gan, T.; Wang, L. L. Layered MoS_2-Graphene Composites for Supercapacitor Applications with Enhanced Capacitive Performance. *Int. J. Hydrogen Energ.* **2013**, *38*, 14027-14034.

(29) Srimuk, P.; Lee, J.; Fleischmann, S.; Choudhury, S.; Jackel, N.; Zeiger, M.; Kim, C.; Aslan, M.; Presser, V. Faradaic Deionization of Brackish and Sea Water via Pseudocapacitive Cation and Anion Intercalation into Few-Layered Molybdenum Disulfide. *J. Mater. Chem. A* **2017,** *5*, 15640-15649.

(30) Kim, H. S.; Cook, J. B.; Lin, H.; Ko, J. S.; to lbert, S. H.;Ozolins, V.; Dunn, B. Oxygen Vacancies Enhance Pseudocapacitive Charge Storage Properties of MoO_{3-X}. *Nat. Mater.* **2017,** *16,* 454-460.

(31) Han, J. L.; Shi, L. Y.; Yan, T. T.; Zhang, J. P.; Zhang, D. S. Removal of Ions from Saline Water Using N, P Co-Doped 3D Hierarchical Carbon Architectures via Capacitive Deionization. *Environ. Sci.: Nano* **2018,** *5*, 2237-2345.

(32) Hu, Z.; Wang, L. X.; Zhang, K.; Wang, J. B.; Cheng, F. Y.; Tao, Z. L.; Chen, J. MoS_2 Nanoflowers with Expanded Interlayers as High-Performance Anodes for Sodium-Ion Batteries. *Angew. Chem. Int.*

419 *Ed. Engl.* **2014,** *53*, 12794-12798.

420 (33) Chang, K.; Chen, W. X. L-Cysteine-Assisted Synthesis of Layered MoS_2/Graphene Composites
421 with Excellent Electrochemical Performances for Lithium Ion Batteries. *ACS Nano* **2011,** *5*, 4720-
422 4728.

423 (34) Li, H. L.; Yu, K.; Fu, H.; Guo, B. J.; Lei, X.; Zhu, Z. Q. MoS_2/Graphene Hybrid Nanoflowers
424 with Enhanced Electrochemical Performances as Anode for Lithium-Ion Batteries. *J. Phys. Chem. C*
425 **2015,** *119*, 7959-7968.

426 (35) Ni, J. F.; Zhao, Y.; Li, L.; Mai, L. Q. Ultrathin MoO_2 Nanosheets for Superior Lithium Storage.
427 *Nano Energy* **2015**, *11*, 129-135.

428 (36) Eda, G.; Yamaguchi. H.; Voiry. D.; Fujita, T.; Chen, M. W.; Chhowalla, M. Photoluminescence
429 from Chemically Exfoliated MoS_2. *Nano Lett.* **2011**, *11*, 5111-5116.

430 (37) Jiang, J. X.; Yang, W. L.; Wang, H.; Zhao, Y.; Guo, J.; Zhao, J. Q.; Beidaghi, M.; Gao, L. J.
431 Electrochemical Performances of MoO_2/C Nanocomposite for Sodium Ion Storage: An Insight Into
432 Rate Dependent Charge/Discharge Mechanism. *Electrochim. Acta* **2017**, *240*, 379-387.

433 (38) Shi, Z. T.; Kang, W. P.; Xu, J.; Sun, Y. W.; Jiang, M.; Ng, T. W.; Xue, H. T.; Yu, D. Y. W.; Zhang,
434 W. J.; Lee, C. S. Hierarchical Nanotubes Assembled from MoS_2-Carbon Monolayer Sandwiched
435 Superstructure Nanosheets for High-Performance Sodium Ion Batteries. *Nano Energy* **2016,** *22*, 27-
436 37.

437 (39) Chang, K.; Mei, Z. W.; Wang, T.; Kang, Q.; Ouyang, S. X.; Ye, J. H. MoS_2/Graphene Cocatalyst
438 for Efficient Photocatalytic H-2 Evolution under Visible Light Irradiation. *ACS Nano* **2014,** *8*, 7078-
439 7087.

440 (40) Gopalakrishnan, D.; Damien, D.; Shaijumon, M. M. MoS_2 Quantum Dot-Interspersed Exfoliated

441 MoS_2 Nanosheets. *ACS Nano* **2014,** *8*, 5297-5303.

442 (41) Zhou, K. G.; Withers, F.; Cao, Y.; Hu, S.; Yu, G. L.; Casiraghi, C. Raman Modes of MoS_2 Used
443 as Fingerprint of Van Der Waals Interactions in 2-D Crystal-Based Heterostructures. *ACS Nano* **2014,**
444 *8*, 9914-9924.

445 (42) Han, J. L.; Chen, G. R.; Yan, T. T.; Liu, H. J.; Shi, L. Y.; An, Z. X.; Zhang, J. P.; Zhang, D. S.
446 Creating Graphene-Like Carbon Layers on SiO Anodes via A Layer-By-Layer Strategy for Lithium-
447 Ion Battery. *Chem. Eng. J.* **2018,** *347*, 273-279.

448 (43) Wang, Z.; Yan, T. T.; Shi, L. Y.; Zhang, D. S. *In Situ* Expanding Pores of Dodecahedron-Like
449 Carbon Frameworks Derived from MoFs for Enhanced Capacitive Deionization. *ACS Appl. Mater.*
450 *Interfaces* **2017,** *9*, 15068-15078.

451 (44) Duan, H. Y.; Yan, T. T.; Li, Z. Y.; Chen, G. R.; Zhang, J. P.; Shi, L. Y.; Zhang, D. S. Rapid Synthesis
452 of Self-Supported Three-Dimensional Bubble-Like Graphene Frameworks as High-Performance
453 Electrodes for Supercapacitors. *Sustain. Energ. Fuels* **2017,** *1*, 1557-1567.

454 (45) Dou, F.; Shi, L. Y.; Song, P. A.; Chen, G. R.; An, J.; Liu, H. J.; Zhang, D. S. Design of Orderly
455 Carbon Coatings for SiO Anodes Promoted by TiO_2 Toward High Performance Lithium-Ion Battery.
456 *Chem. Eng. J.* **2018,** *338*, 488-495.

457 (46) An, J.; Shi, L. Y.; Chen, G. R.; Li, M. S.; Liu, H. J.; Yuan, S.; Chen, S. M.; Zhang, D. S. Insights
458 into The Stable Layered Structure of A Li-Rich Cathode Material for Lithium-Ion Batteries. *J. Mater.*
459 *Chem. A* **2017,** *5*, 19738-19744.

460 (47) Jung, H. H.; Hwang, S. W.; Hyun, S. H.; Kang-Ho, L.; Kim, G. T. Capacitive Deionization
461 Characteristics of Nanostructured Carbon Aerogel Electrodes Synthesized via Ambient Drying.
462 *Desalination* **2007,** 216, 377-385.

463 (48) Wang, H.; Shi, L. Y.; Yan, T. T.; Zhang, J. P.; Zhong, Q. D.; Zhang, D. S. Design of Graphene-
464 Coated Hollow Mesoporous Carbon Spheres as High Performance Electrodes for Capacitive
465 Deionization. *J. Mater. Chem. A* **2014,** 2, 4739-4750.
466 (49) Mayes, R. T.; Tsouris, C.; Kiggans, J. O.; Mahurin, S. M.; Depaoli, D. W.; Dai, S. Hierarchical
467 Ordered Mesoporous Carbon from Phloroglucinol-Glyoxal and Its Application in Capacitive
468 Deionization of Brackish Water. *J. Mater. Chem.* **2010,** *20*, 8674-8678.
469 (50) Dykstra, J. E.; Zhao, R.; Biesheuvel, P. M.; Van Der Wal, A. Resistance Identification and Rational
470 Process Design in Capacitive Deionization. *Water Res.* **2016,** *88*, 358-370.
471 (51) El-Deen, A. G.; Choi, J. H.; Kim, C. S.; Khalil, K. A.; Almajid, A. A.; Barakat, N. A. M. TiO_2
472 Nanorod-Intercalated Reduced Graphene Oxide as High Performance Electrode Material for
473 Membrane Capacitive Deionization. *Desalination* **2015,** 361, 53-64.
474 (52) Srimuk, P.; Zeiger, M.; Jackel, N.; to losa, A.; Kruner, B.; Fleischmann, S.; Grobelsek, I.; Aslan,
475 M.; Shvartsev, B.; Suss, M. E.; Presser, V. Enhanced Performance Stability of Carbon/Titania Hybrid
476 Electrodes During Capacitive Deionization of Oxygen Saturated Saline Water. *Electrochimica Acta*
477 **2017,** 224, 314-328.
478 (53) Shi, W. B.; Zhou, X. C.; Li, J. Y.; Meshot, E. R.; Taylor, A. D.; Hu, S.; Kim, J. H.; Elimelech, M.;
479 Plata, D. L. High-Performance Capacitive Deionization via Manganese Oxide Coated, Vertically
480 Aligned Carbon Nanotube. *Environ. Sci. Tech. Let.* **2018,** 5, 692-700.
481 (54) Byles, B. W.; Cullen, D. A.; More, K. L.; Pomerantseva, E. Tunnel Structured Manganese Oxide
482 Nanowires as Redox Active Electrodes for Hybrid Capacitive Deionization. *Nano Energy* **2018,** 44,
483 476-488.
484 (55) Srimuk, P.; Lee, J.; Fleischmann, S.; Choudhury, S.; Jackel, N.; Zeiger, M.; Kim, C.; Aslan, M.;

485 Presser, V. Faradaic Deionization of Brackish and Sea Water *via* Pseudocapacitive Cation and Anion
486 Intercalation into Few-Layered Molybdenum Disulfide. *J. Mater. Chem. A* **2017**, *5*, 15640-15649.
487 (56) Dykstra, J. E.; Keesman, K. J.; Biesheuvel, P. M.; Van Der Wal, A. Theory of pH Changes in
488 Water Desalination by Capacitive Deionization. *Water Res.* **2017,** *119*, 178-186.
489 (57) Kang, Y.; Pyo, S.; Jo, S.; Kim, J. Light-Assisted Recovery of Reacted MoS_2 for Reversible NO_2
490 Sensing at Room Temperature. *Nanotechnology* **2019,** *30*, 355504.
491 (58) Yang, C. X.; Wang, B.; Xie, Y. N.; Zhang, Y. F.; Jin, C. H. Deriving MoS_2 Nanoribbons from Their
492 Flakes by Chemical Vapor Deposition. *Nanotechnolog y* **2019,** *30*, 255602.
493 (59) Zhang, X.; Liang, Y. Y. Nickel Hydr(oxy)oxide Nanoparticles on Metallic MoS_2 Nanosheets: A
494 Synergistic Electrocatalyst for Hydrogen Evolution Reaction. *Adv. Sci.* **2018**, *5*, 1700644.
495 (60) Xuyen, N. T.; Ting, J. M. Hybridized 1T/2H MoS_2 Having Controlled 1T Concentrations and its
496 use in Supercapacitors. *Chem-Eur J.* **2017**, *23,* 17348-17355.
497 (61) Calandra, M. Chemically exfoliated single-layer MoS_2: Stability, lattice dynamics, and catalytic
498 adsorption from first principles. *Phys. Rev. B* **2013**, *88,* 245428.
499

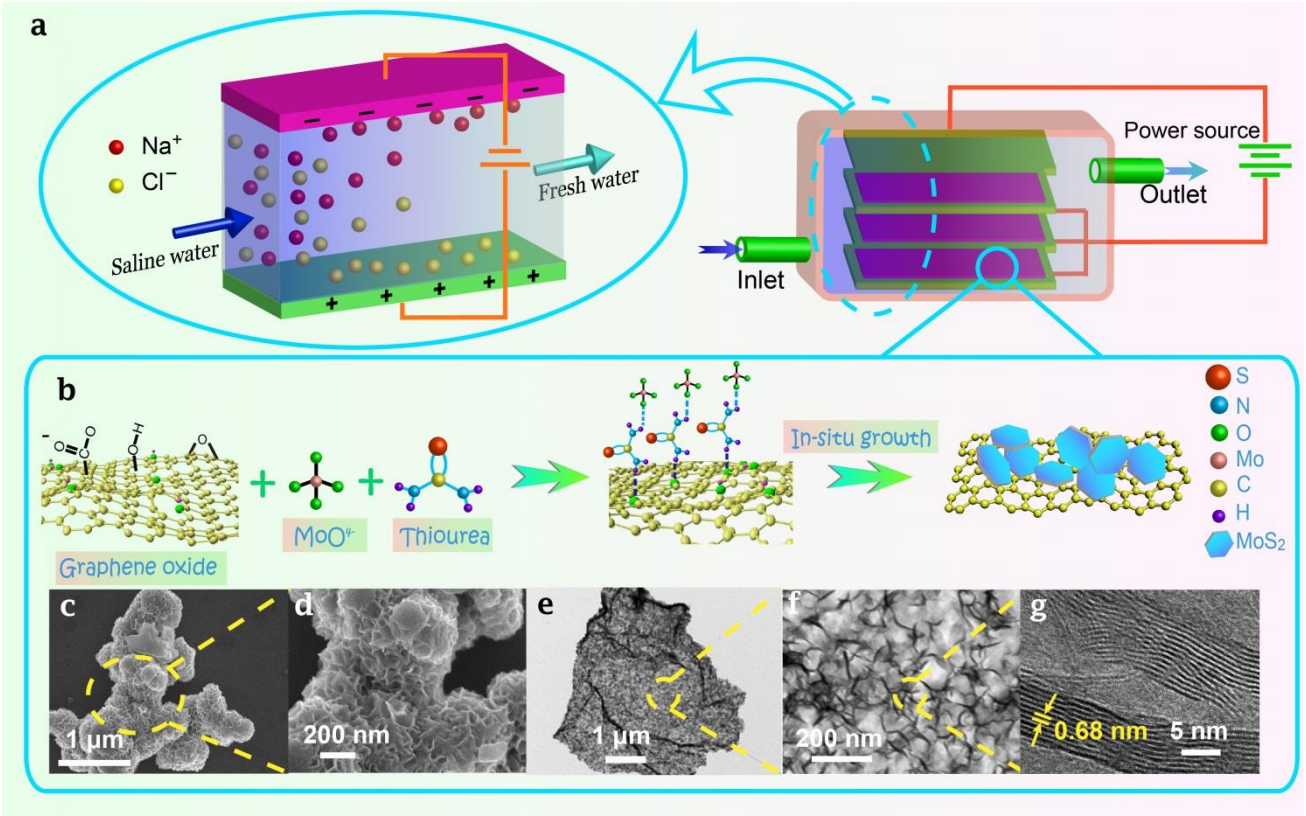

500

501 **Figure 1.** (a) Schematic illustration of CDI device; (b) Schematic illustration of preparation of MoS_2-graphene

502 hybrids; (c and d) SEM images of MG-1.6; (e and f) TEM images of MG-1.6; (g) HRTEM image of MG-1.6.

503

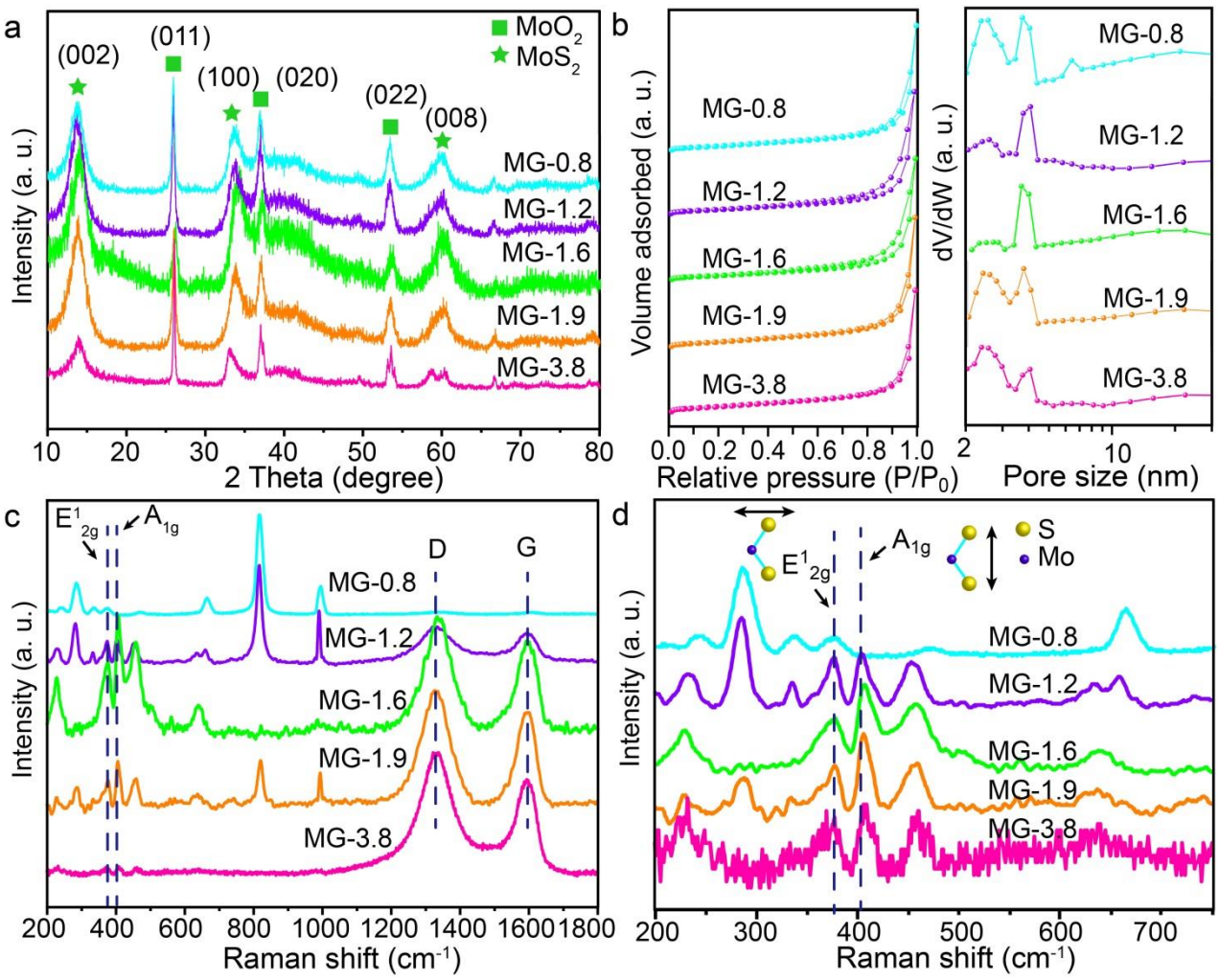

Figure 2. (a) XRD patterns, (b) N_2 adsorption-desorption isotherms (left) and BJH pore size distribution profiles (right), (c) full Raman spectra and (d) local-magnified Raman spectra of different samples.

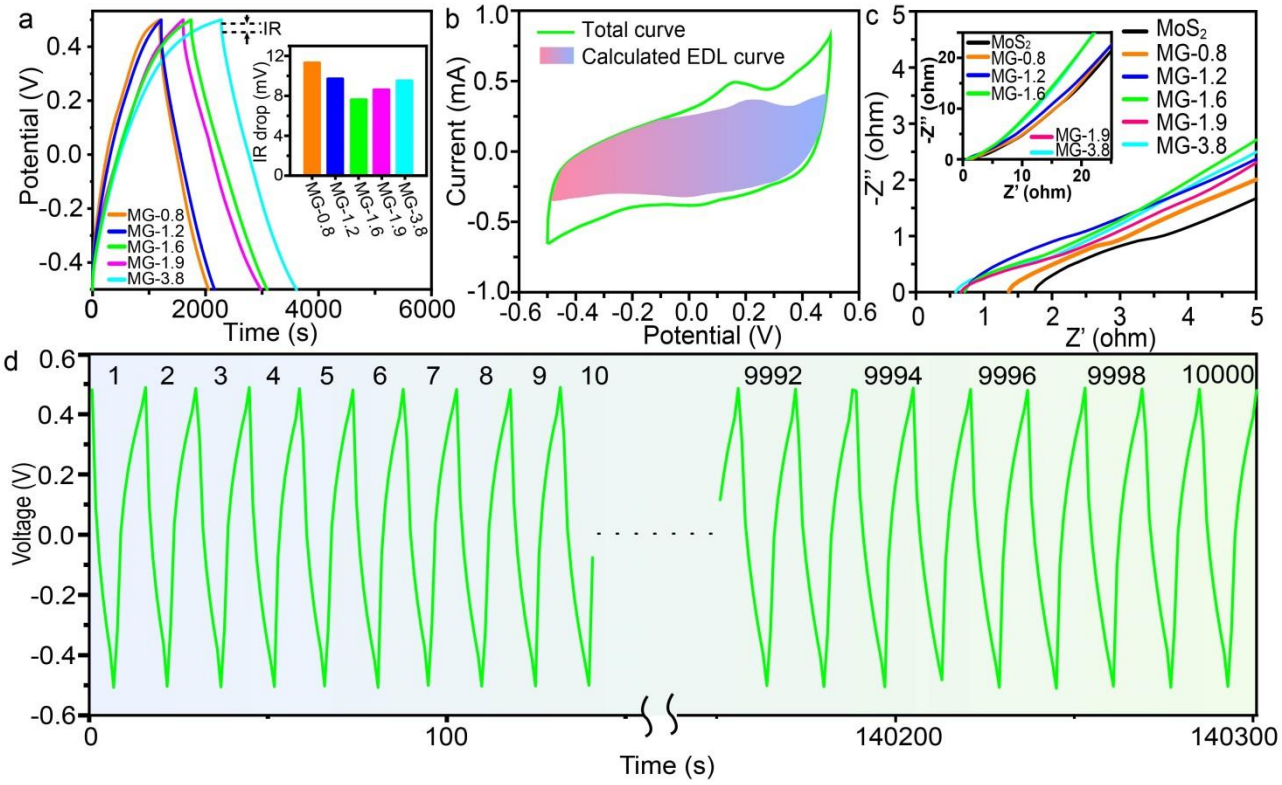

507

508 **Figure 3.** (a) GCD curves at a current density of 0.2 A/g (the inset is IR drop of different samples); (b) CV curves at

509 a scanning rate of 0.2 mV/s (the shadow is the calculated capacitive charge); (c) EIS curves of different samples (the

510 inset is the full EIS); and (d) Long GCD cycles of MG-1.6 at a current density of 5 A/g.

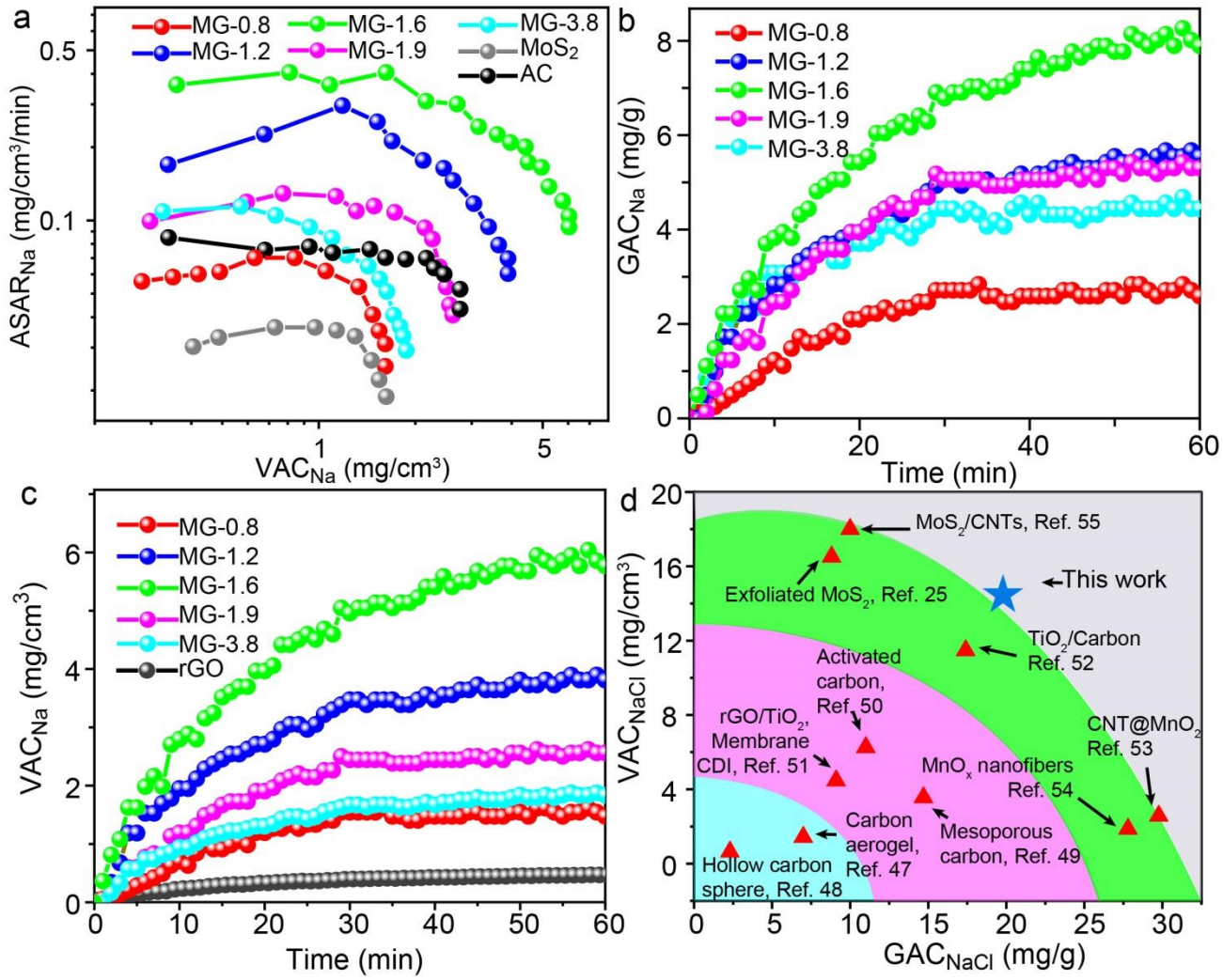

Figure 4. (a) Ragone curves of different samples in a 500 mg/L NaCl aqueous solution at 1.2 V and 60 mL/min; (b) Plots of GAC_{Na} *vs.* deionization time of different samples in a 500 mg/L NaCl aqueous solution at 1.2 V and 60 mL/min; (c) Plots of VAC_{Na} *vs.* deionization time of different samples in a 500 mg/L NaCl aqueous solution at 1.2 V and 60 mL/min; and (d) Comparison of VAC_{NaCl} and GAC_{NaCl} between the reported materials and material of this work.

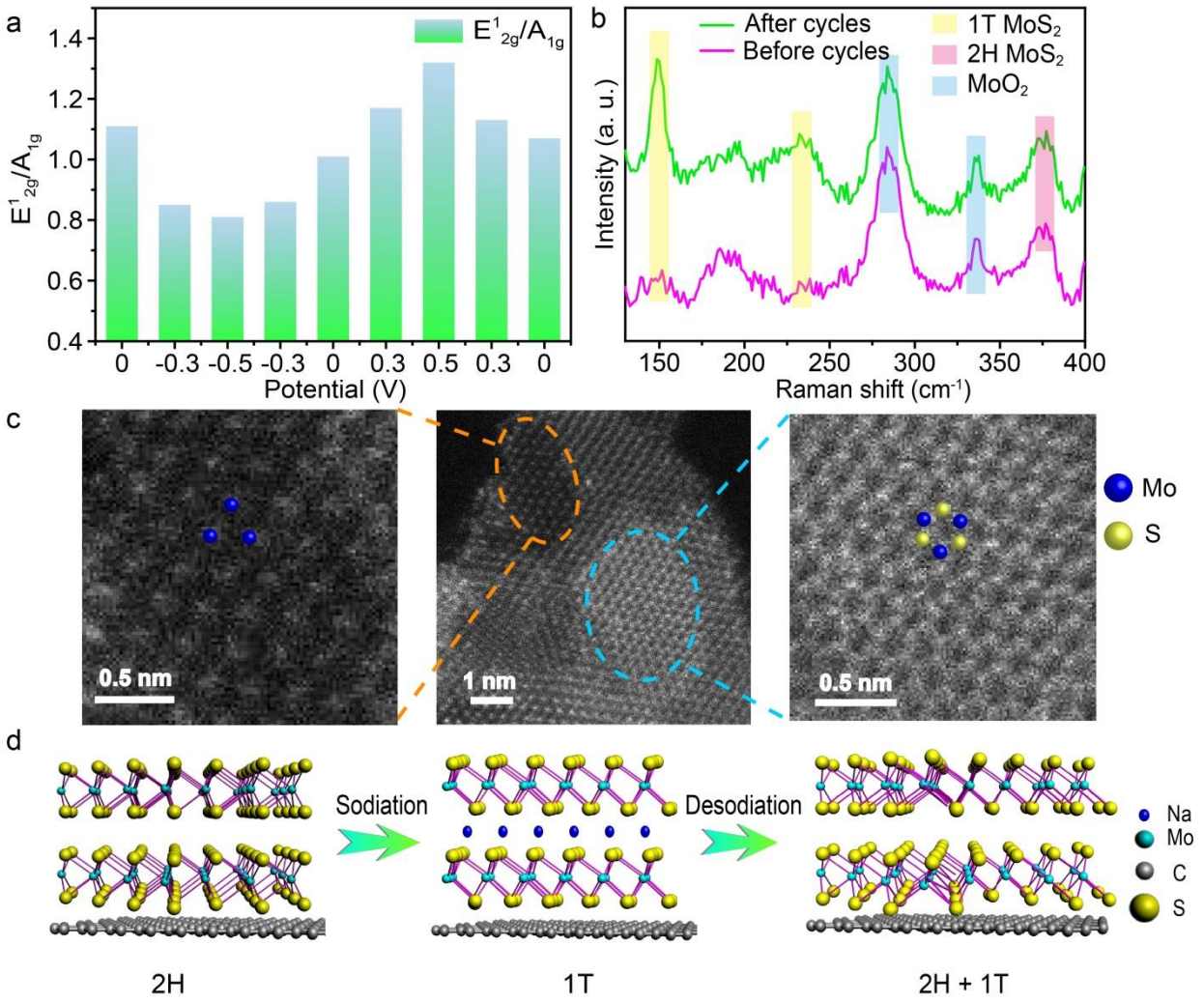

Figure 5. (a) *In-situ* Raman spectra peak ratio of E^1_{2g}/A_{1g} of MG-1.6 during a CV cycle range from -0.5 V to 0.5 V ; (b) Raman spectra of MG-1.6 before and after 50 cycles; (c) HAADF-STEM images of MG-1.6 after 50 CDI cycles (the left image corresponding to 1T MoS_2, the right image corresponding to 2H MoS_2); and (d) Schematic illustration of sodiation and desodiation of 2H MoS_2.

523 **Table 1.** Comparison of between reported CDI electrodes and this work.

Materials	GAC_{NaCl} (mg/g)	VAC_{NaCl} (mg/cm^3)	Reference
MoS_2-graphene	19.4	14.3	This work
Carbon aerogel	~7	1.43	47
Hollow Carbon sphere	2.3	0.64	48
Mesoporous carbon	14.7	3.56	49
Activated carbon	11	6.26	50
reduced GO/TiO_2	9.1	4.47	51
TiO_2/Carbon	17.4	11.47	52
Carbon nanotube@MnO_2	29.77	2.57	53
MnO_x nanofiber	27.8	1.87	54
MoS_2/Carbon nanotube	10	18	55
Exfoliated MoS_2	8.81	16.51	25

524

525

526 **TOC**

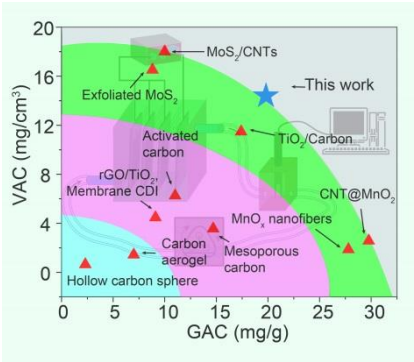

527